

# AIAA'87

*AST*  
A.2.5

**AIAA-87-1293**

**High Resolution Calculations of  
Unsteady, Two-Dimensional Non-  
equilibrium Gas Dynamics with  
Experimental Comparisons**

H.M. Glaz, Univ. of Maryland, College  
Park, MD; P. Colella, Lawrence Liver-  
more National Lab., Livermore, CA;  
J.P. Collins and R.E. Ferguson, Naval  
Surface Weapons Center, Silver  
Spring, MD

**AIAA 19th Fluid Dynamics, Plasma  
Dynamics and Lasers Conference**

June 8-10, 1987/Honolulu, Hawaii

HIGH RESOLUTION CALCULATIONS OF UNSTEADY, TWO-DIMENSIONAL NONEQUILIBRIUM  
GAS DYNAMICS WITH EXPERIMENTAL COMPARISONS

Harland M. Glaz\*  
Mathematics Dept.  
University of Maryland  
College Park, MD 20742

Phillip Colella\*\*  
Lawrence Livermore National Laboratory  
Mail Stop L306  
Livermore, CA 94550

James P. Collins<sup>+</sup> and Ralph E. Ferguson<sup>+</sup>  
Applied Mathematics Branch (R44)  
Naval Surface Weapons Center  
White Oak  
Silver Spring, MD 20903-5000

Abstract

The Eulerian second-order Godunov scheme is extended to treat a mixture of nonequilibrium, chemically reacting gases. We consider only the case of high temperature air here, although the scheme is more generally applicable. Several planar oblique shock wave calculations are discussed, including direct comparison with experimental data. The new results are an improvement over our previous gas dynamics calculations for the same problems.

Introduction

Oblique shock wave reflection is a benchmark problem both for more complex physical and engineering problems and for validation of compressible flow computer codes.<sup>1</sup> This problem has proven amenable to accurate experimental measurement in shock tubes and data is readily available in the literature. Also, the complex wave structure in the Mach stem region of these experiments closely resembles the flowfield phenomenology of typical applications. Finally, assuming inviscid gas dynamics, no length scale is present in the problem which has made it possible to propose analytical theories for important issues such as shock structure transition.<sup>2</sup>

The large shock tube temperatures and pressures which are obtained for shock wave Mach numbers ( $M_s$ ) greater than about five necessitate low ambient density test gases (a few percent of atmospheric) for such experiments. Consequently, vibrational mode excitation can occur and the associated relaxation length scale is comparable to hydrodynamic scales, e.g., the distance between the first and second triple point in a double Mach reflection or the triple point height above the wedge surface. Additionally, if  $M_s$  is somewhat larger, the flowfield temperature is high enough (either behind the incident or reflected shock, or both) to introduce dissociation-recombination reactions in appropriate test gases; the postshock relaxation of the gas to its equilibrium value introduces other length scales, also comparable to hydrodynamic features.

High resolution calculations of oblique shock wave reflection flowfields using the Eulerian second-order Godunov scheme for gas dynamics have been previously reported.<sup>1-8</sup> These studies were inviscid and used (imperfect) equilibrium equations-of-state (EOS) to model high temperature effects in the various gases. The agreement between experimental and computational results is excellent in these papers; however, real gas Navier-Stokes calculations are required to fully reproduce the flowfield phenomenology resulting from relaxation effects and the viscous boundary layer, and to obtain better quantitative agreement.<sup>1,2</sup>

The purpose of this paper is to report an extension of our numerical approach to nonequilibrium, reactive gas mixtures applicable to multidimensional, high temperature air flowfields. Our calculations are compared with experimental results obtained by I. I. Glass and his colleagues using the shock tube facility at the University of Toronto, Institute for Aerospace Studies (UTIAS)<sup>2</sup>. For the cases studied here, the test gas is air and the shocks are sufficiently strong to induce significant vibrational nonequilibrium in critical regions of the flowfield; we are also able to validate substantial chemistry effects in some of the cases.

The high temperature air model used here is expected to be valid only to temperatures up to 8000 - 9000°K, since we only include vibrational excitation and a dissociation-recombination reaction mechanism. However, the algorithm could be extended to include additional physical effects such as ionization. In particular, we expect that the mathematical structure supports the physics needed for applications in reentry aerodynamics.

Oblique Shock Wave Reflection

The configuration for oblique shock wave reflection is illustrated in Figures 1 and 2. In Figure 1, a planar shock wave of shock wave Mach number  $M_s$  approaches, through quiescent gas, the wedge corner which is set at an angle  $\theta$  with respect to the incoming flow. For inviscid, equilibrium flow, there is no length scale in the problem which implies that the

\*Associate Professor, Member AIAA

\*\*Group Leader, Applied Mathematics Group

<sup>+</sup>Mathematician

solution depends only on  $x/t$  and  $y/t$  (where the wedge corner is taken as the origin of coordinates), and the resulting flowfields are called pseudosteady or self-similar. The possible solutions<sup>2</sup> are illustrated in Figure 2; they are functions of  $M_s$ ,  $\theta_w$ , the EOS of the gas, and, for a nonpolytropic EOS, the preshock state of the gas.<sup>1,2</sup>

The data obtained from the UTIAS facility is in the form of infinite fringe interferograms of the flowfield, obtained with a 23 cm diameter field of view Mach-Zender interferometer.<sup>7</sup> The density jump,  $\Delta\rho$ , between fringes in the interferogram is a constant, thereby allowing for easy data reduction. However, the shock<sup>7</sup> jump conditions must be evaluated to obtain states (1), (2), (3) at the triple point since the fringes inside the shock waves cannot be resolved. For a frozen or equilibrium jump, this problem is straightforward given an accurate measurement of the triple point angle,  $\chi$ .<sup>2,7,8,9</sup>

Relaxation processes introduce two characteristic signatures into the interferograms. First, the relaxation zone behind the incident shock is readily apparent. Second, the fringes behind the reflected shock are nearly tangentially incident at the shock. Of course, the physical mechanisms responsible for the relaxation effects cannot be discerned from the interferograms alone and additional analysis or computation is required. With relaxation processes present, length scales are introduced and the solution is no longer self-similar. Among other effects, it becomes possible for the triple point angle,  $\chi$ , to be time-dependent. Also, it is possible that the shock layers in the problem are only partially frozen at scales resolvable in the interferograms. As a consequence, the triple point analysis using either frozen or equilibrium jump conditions may introduce errors into the data reduction.

If  $\ell$  represents a relaxation length scale and  $L$  (see Figure 2) a hydrodynamic scale,  $\ell \gg L$ ,  $\ell \sim L$ ,  $\ell \ll L$  represent frozen, nonequilibrium, and equilibrium flow, respectively. A time-dependent experiment or calculation runs through each of the three regimes in succession as  $t \rightarrow \infty$ . It has been convincingly shown that significant flowfield features (e.g.,  $\chi$ ) differ substantially in the two asymptotic regimes which can be studied by gas dynamic computations.<sup>1,3,4</sup> The problems studied here are all in the nonequilibrium regime.

### Equations of Motion

High temperature air is modelled as a nonequilibrium, reacting mixture of gases. For the conditions (i.e., temperature range) treated in this paper, and ignoring ionization reactions, the governing equations in conservation form are<sup>10</sup>:

$$\dot{q}_t^\alpha + \nabla \cdot (\rho^\alpha \underline{u}) = \dot{w}^\alpha; \quad \alpha = 1, \dots, N \quad (1)$$

$$(\rho \underline{u})_t + \nabla \cdot (\rho \underline{u} \underline{u} + p) = 0 \quad (2)$$

$$(\rho E)_t + \nabla \cdot (\rho \underline{u} E + p \underline{u}) = -\sum_\alpha \dot{w}^\alpha (\Delta h_f^\circ)^\alpha \quad (3)$$

$$(\rho^\alpha q^\alpha)_t + \nabla \cdot (\rho^\alpha q^\alpha \underline{u}) = \rho^\alpha \dot{q}^\alpha; \quad \alpha = 1, \dots, N \quad (4)$$

where  $\rho^\alpha$  = density of species  $\alpha$ ,  $\rho$  = mixture density =  $\sum_\alpha \rho^\alpha$ ,  $\underline{u}$  = velocity,  $p$  = pressure,  $E$  = total energy per unit mass,  $q^\alpha$  = vibrational energy per unit mass of species  $\alpha$ ,  $(\Delta h_f^\circ)^\alpha$  = specific heat of formation at 0°K of species  $\alpha$ , and  $N$  = total number of species present. The source terms  $\dot{w}^\alpha$  and  $\dot{q}^\alpha$  represent the production of species  $\alpha$  through chemical reaction and the relaxation of vibrational energy of species  $\alpha$  to its equilibrium value, respectively.

The pressure is given by the equation-of-state

$$p = \bar{\rho} \bar{R} T \quad (5)$$

where  $T$  = temperature,  $\bar{R} = R/M$ ,  $R$  = universal gas constant,  $M = (\sum_\alpha c^\alpha / M^\alpha)^{-1}$ ,  $M^\alpha$  = molecular weight of species  $\alpha$ , and  $c^\alpha$  = mass fraction of species  $\alpha = \rho^\alpha / \rho$ . The total specific energy is

$$E = e + 1/2 \underline{u}^2 \quad (6)$$

where  $e$  = specific internal energy of the mixture, i.e.,  $e = \sum_\alpha c^\alpha e^\alpha$  with  $e^\alpha$  = specific internal energy of species  $\alpha$ ,

$$e^\alpha = (\gamma^\alpha - 1)^{-1} R^\alpha T + q^\alpha \quad (7)$$

Here,  $R^\alpha = R/M^\alpha$  and  $\gamma^\alpha$  = polytropic index for species  $\alpha$  (= 7/5 for diatomic species and 5/3 for monatomic species). The first term on the right-hand side of (7) represents the contribution of translational and rotational modes (which are assumed to be in equilibrium) to the internal energy. It follows from (7) that

$$T = (e - \sum_\alpha c^\alpha q^\alpha) / \sum_\alpha \frac{c^\alpha R^\alpha}{\gamma^\alpha - 1} \quad (8)$$

Substituting (8) in (5), one easily sees that the pressure is a function of the conserved quantities.

Conservation of mass implies that

$$\rho_t + \nabla \cdot (\rho \underline{u}) = 0, \quad (9)$$

i.e.,  $\sum_\alpha \dot{w}^\alpha = 0$ . Equations (1) and (4) can be recast for smooth flow into the characteristic forms

$$c_t^\alpha + \underline{u} \cdot \nabla c^\alpha = \rho^{-1} \dot{w}^\alpha; \quad \alpha = 1, \dots, N \quad (10)$$

$$(c^\alpha q^\alpha)_t + \underline{u} \cdot \nabla (c^\alpha q^\alpha) = c^\alpha \dot{q}^\alpha; \quad \alpha = 1, \dots, N \quad (11)$$

Note that  $\sum_\alpha c^\alpha = 1$  and that only  $N$  of the  $N+1$  equations (9), (10) are independent.

For high temperature air without ionization, it is a reasonable approximation<sup>11</sup> to take  $N=5$  corresponding to the species  $O_2$ ,  $N_2$ ,  $NO$ ,  $O$ , and  $N$ . Following Ref. 11, we assume that the reaction mechanism consists of  $R$  elementary reactions of the form



where  $X_{\alpha}$  = molar concentration of species  $\alpha$ ,  $v'_{\alpha}$  and  $v''_{\alpha}$  are the stoichiometric coefficients for species  $\alpha$  in reaction  $r$ , and  $k_{f,r}$  and  $k_{b,r}$ , which are experimentally determined explicit functions of  $T$ , are the forward and backward reaction rates, respectively. The production terms are<sup>11</sup>

$$\dot{w}^{\alpha} = M^{\alpha} \dot{X}_{\alpha}; \quad \alpha = 1, \dots, N \quad (13)$$

where

$$\dot{X}_{\alpha} = \sum_{r=1}^R (v''_{\alpha,r} - v'_{\alpha,r}) \dot{\omega}_r \quad (14)$$

$$(k_{f,r}(T) \prod_{s=1}^N X_s^{v'_{s,r}} - k_{b,r}(T) \prod_{s=1}^N X_s^{v''_{s,r}})$$

For the calculations presented in this paper, the reaction mechanism and the functional form of  $k_{f,r}$ ,  $k_{b,r}$  follow the data given by C.

Park,<sup>12,13</sup>

Finally, relaxation of vibrational energy is modelled by

$$\dot{q}^{\alpha} = \frac{q^{*\alpha}(T) - q^{\alpha}}{\tau^{\alpha}(p,T)}; \quad \alpha = O_2, N_2, NO \quad (15)$$

where  $q^{*\alpha}(T)$  = equilibrium vibrational energy per unit mass of species  $\alpha$  at temperature  $T$  and  $\tau^{\alpha}$  = relaxation time. The monatomic species  $O$ ,  $N$  do not possess vibrational modes, so  $q^{\alpha} \equiv 0$  for  $\alpha = O, N$ . These terms are given explicitly by<sup>11</sup>

$$q^{*\alpha}(T) = \frac{R \theta_0^{\alpha}}{\exp(\theta_0^{\alpha}/T) - 1}; \quad \alpha = O_2, N_2, NO \quad (16)$$

where  $\theta_0^{\alpha}$  = vibrational temperature for species  $\alpha$ , and

$$\tau^{\alpha}(p,T) = \frac{B^{\alpha} \exp[(k^{\alpha}/T)^{1/3}]}{p} \quad (17)$$

The equation for  $\tau^{\alpha}$  is an approximate form of the Landau-Teller equation valid in the temperature range considered here.<sup>11</sup> The constants  $B^{\alpha}$ ,  $k^{\alpha}$  must be experimentally determined; we are using the data from Ref. 11 with the additional approximation that the heat bath molecule for species  $\alpha$  is taken to be species  $\alpha$  (in general, the constants depend on the collision partner).

## Numerical Method

An operator splitting approach has been implemented in which the gas dynamics with frozen chemistry is solved for  $\Delta t$ , alternately with the chemistry advanced  $\Delta t$  at constant volume and ignoring spatial gradients. The time step  $\Delta t$  is chosen to satisfy the CFL condition for the gas dynamic scheme alone. For general reactive flow problems, such a method potentially introduces large errors due to the ignored hydrodynamic-chemistry interactions over a time step, unless the spatial mesh in reaction regions is small enough to bring the two time scales into balance. Our working hypothesis for the present work is that, since both the vibrational relaxation and dissociation-recombination processes are tending to equilibrium without large oscillations, the method will be accurate on length scales greater than a few mesh points, even on relatively coarse meshes.

The hydrodynamic step is solved with a version of the Eulerian second-order Godunov scheme.<sup>4</sup> This scheme is directionally split, so we discuss the method for solving one-dimensional gas dynamics in Cartesian coordinates. A brief summary of the method is as follows: (1) characteristic variables are selected and high-order, monotonic slopes are constructed for them in each computational zone, (2) left and right states at each zone interface are constructed by applying characteristic projection operators to the profiles constructed in the first step, (3) the zone interface Riemann problems are solved, and (4) interface fluxes are evaluated and a conservative differencing step performed. The modifications necessary to generalize the single phase method to a gas mixture satisfying eqns. (1) - (8) are straightforward, as indicated below (the ensuing discussion assumes familiarity with Ref. 4).

There are several natural choices for characteristic variables, e.g.,  $v^1 =$

$$(\rho^1, \dots, \rho^N, u, p, q^1, \dots, q^N)^T, \quad v^2 = (\tau, \rho^1, \dots,$$

$\rho^{N-1}, u, p, q^1, \dots, q^N)^T, \quad \tau = \rho^{-1}$ , etc. For the present study, we have chosen

$$v = (\tau, c^1, \dots, c^N, u, p, q^1, \dots, q^N)^T \quad (18)$$

subject to the constraint  $\sum_{\alpha} c^{\alpha} = 1$  everywhere; the constraint allows us to both retain  $\tau$  and not single out any of the  $c^{\alpha}$  in the characteristic transport step. For this choice, the characteristic equations for the variables  $c^{\alpha}, q^{\alpha}, \alpha = 1, \dots, N$  (see eqns. (10), (11)) decouple from the rest of the system. Consequently, the computation of the characteristic projection operators is almost exactly as described in Ref. 4, and they have the same properties. The mixture Riemann problem has essentially the same solution as that for single fluid gas dynamics. This is so because the quantities  $c^{\alpha}, q^{\alpha}$  are advected along streamlines and do not jump across the nonlinear waves (shock waves and rarefaction waves) in the Riemann problem solution. Thus, only  $\tau, u$ , and  $p$  vary across the left and right waves and the

Rankine-Hugoniot conditions are as in the single fluid case. If  $\gamma$  is defined via  $p = (\gamma - 1)\rho(e - \sum_{\alpha} q^{\alpha})$ , it is easy to check that  $\gamma$  also does not jump across nonlinear waves. Also,  $\Gamma = \gamma$  where the "sound speed gamma" is defined by  $c^2 = \Gamma p$ ,  $c =$  (frozen) sound speed. Of course, the value of  $\gamma$  is different in the left and right states defining the Riemann problem. The end result is that the nonlinear secant iteration and the sampling procedure to obtain interface values is identical to that described in Ref. 4, save for the additional bookkeeping required to keep track of all of the components of  $v$ .

The set of equations solved in the chemistry step of the operator splitting algorithm is

$$\frac{dc^{\alpha}}{dt} = \rho^{-1} M^{\alpha} \chi_{\alpha}^{\alpha}; \quad \alpha = 1, \dots, N \quad (19)$$

$$\frac{d(c^{\alpha} q^{\alpha})}{dt} = c^{\alpha} \frac{q^{\alpha}(T) - q^{\alpha}}{\tau^{\alpha}(p, T)}; \quad \alpha = N_2, O_2, NO \quad (20)$$

$$\frac{de}{dt} = \rho^{-1} \sum_{\alpha} (M^{\alpha} (\Delta h_f^{\alpha})) \chi_{\alpha}^{\alpha}. \quad (21)$$

This is a system of  $N+4$  coupled nonlinear ordinary differential equations; note that  $T$ ,  $p$  are explicit functions of  $c^{\alpha}$ ,  $c^{\alpha} q^{\alpha}$ ,  $\alpha = 1, \dots, N$ , and  $e$  according to the relations (5) and (8). They are in a form suitable for solution by standard numerical methods. In our calculations, we have used standard explicit solvers such as 2nd and 4th order Runge-Kutta methods or Euler's method. The chemistry time step was taken small enough to insure accuracy. In future work, we intend to explore implicit methods, stiff solvers, and various approximation schemes which take advantage of the fact that, for much numerical work, accuracy at levels higher than the hydrodynamic scheme may not be useful.

#### Initial and Boundary Conditions

A square mesh aligned with the wedge surface (Figure 1) is used. The ambient state,  $U_0$ , is taken to consist of 79%  $N_2$  and 21%  $O_2$  at density  $\rho_0$  and pressure  $p_0$  corresponding to the experimental data<sup>3</sup> for each calculation. The postshock state,  $U_1$ , is obtained by solving the Rankine-Hugoniot conditions with an additional equation enforcing vibrational equilibrium. The jump is then conservatively interpolated onto the mesh, and the calculation runs to completion without further intervention.

The structure of the one-dimensional incident shock is an important issue in our analysis of the results. The reactive flow calculations exhibit an "overshoot" behind the shock prior to downstream relaxation to equilibrium (and this has been verified by long-time calculations on a one-dimensional mesh); this phenomenon may well be physical. Nevertheless, a small amplitude disturbance is introduced into the flow behind the reflected

shock at the second triple point by the overshoot. The calculated incident shock is partially reactive on scales of the order of a few mesh points whereas the data reduction for the experiment assumes a frozen jump; on the fine meshes used here, the error introduced by this difference is small and would be made smaller by refining the mesh still further. Both of these issues can be resolved by using another version of the Godunov scheme in which the incident shock is treated as a tracked front;<sup>14</sup> this will be the subject of further work, along with computing the exact steady shock structure (for both frozen and partial reaction jumps) by quadrature.

The only nontrivial boundary condition is at the top. We have implemented a "Dirichlet" condition in which a discontinuous jump is imposed at the (known) intersection of the incident shock with the top boundary. The postshock state is chosen to be the currently available value from the downstream edge of the state (1) region (the reaction process continues here throughout the calculation). The boundary has been taken far enough away from the reflected shock so that the error introduced by this procedure is negligible. Nevertheless, for reasons of efficiency, we expect to implement a true Dirichlet condition (see, e.g., the treatment in Ref. 15) in future work.

For the meshes used in obtaining the results, the length  $L$  (see Figure 2) corresponds to 350-400 zones, and the vertical distance between the wedge surface and the top of the reflected shock contains between 60 and 100 zones. This is comparable, but somewhat coarser, than the meshes used in Ref. 3. The mesh interval,  $\Delta x = \Delta y$ , is chosen so that at the end of the calculation,  $L$  corresponds closely to the experiment.

#### Results

Results have been obtained for three cases: (I)  $M_S = 7.19$ ,  $\theta_w = 20^\circ$ , (II)  $M_S = 8.70$ ,  $\theta_w = 27^\circ$ , and (III)  $M_S^w = 8.86$ ,  $\theta_w = 20^\circ$ . Two calculations have been performed for each of the cases--a vibrationally relaxing, nonreactive calculation and a vibrationally relaxing, reactive calculation. A direct comparison of the flowfield density contour levels of these computations with experimental data and previously reported calculations<sup>3</sup> with an equilibrium EOS is made in Figures 3, 4, and 5 for the three cases. The EOS used in the gas dynamic calculation is a modified version of the Hansen EOS.<sup>16</sup> The overall structure of the configurations may be discerned by comparing the triple point angles  $\chi$ ,  $\chi'$  and  $\delta =$  corner attachment angle (in degrees; all measurements are by hand):

	$x$	$x'$	$\delta$
I: exp.	11.5		32.0
Hansen	12.0		29.5
VR	12.4		31.5
CR+VR	11.6		31.0
II: exp.	7.5	7.8	23.0
Hansen	9.6	9.0	33.5
VR	10.0	10.2	31.5
CR+VR	8.2	8.5	24.0
III: exp.	10.0	11.2	21-23
Hansen	12.2	12.5	27.0
VR	12.4	13.2	28.5
CR+VR	10.4	11.4	23.6

It is quite clear that the comparison improves substantially as one moves down the page in these figures; the degree of tangential incidence of the contours at the reflected shock improves and matches the interferogram in the reactive case, and the table above shows that wave structure fidelity requires reactive flow calculations (since the Hansen EOS includes reaction effects, it can actually be better than a relaxing, nonreactive model). For Cases II and (especially) III, a wave is introduced into the disturbed flow at  $T'$  which is not present in the experiment; this small amplitude disturbance is caused either by an overshoot behind the incident shock wave or the error in our top boundary condition procedure. Quantitatively, the contours are off by about two levels. It is possible that this can be fully explained by the assumption of a frozen triple point in the data reduction for the interferogram. None of the new calculations match this condition on scales comparable with the mesh. Whether a substantial mesh refinement (or a tracked incident shock) is required for convergence, or whether the experimental incident shock should be taken as partially relaxed/reactive is not clear.

Wall density plots for the calculations are presented in Figure 6. The "wall heating" numerical layer, already present for gas dynamic results,<sup>1,3</sup> is intensified here (this is easily seen in the contour plots, as well) and we have sometimes used the results from the second row of zones above the wedge surface. For Case I, it may be noted that there is a mismatch between the data points in state 1' and the value computed for this state in the calculations. An additional computation was made in which agreement for this value was forced and these results are presented as well. In light of these factors, the agreement is good overall and some of the remaining discrepancies can be analyzed in terms of boundary layer effects in the experiments.<sup>1,3</sup>

Details of the Mach stem region are illustrated in Figure 7. These plots illustrate the rich structure of the mixing processes induced by the wall jet-vortex rollup interaction<sup>1</sup> in this part of the flowfield.

#### Acknowledgements

The authors gratefully acknowledge the permission of Jacob Krispin to use parts of his reaction rate software here. The programming

work of Mike Lijewski was also an important contribution. Discussions with John Anderson, Robert Deschambault, Forrest Gilmore, Irvine Glass, and Jacob Krispin were extremely valuable to us in our work here.

The financial assistance received from the U. S. Department of Energy at the Lawrence Livermore National Laboratory under Contract W-7405-ENG-48; from the U. S. Defense Nuclear Agency under DNA Task Code/Work Unit RARG-00068; and from the Naval Surface Weapons Center Independent Research Fund is acknowledged with thanks.

#### References

1. Glaz, H. M., Colella, P., Glass, I. I., and Deschambault, R. L., "A numerical study of oblique shock-wave reflections with experimental comparisons," Proc. R. Soc. Lond. A 398 (1985), pp. 117-140.
2. Glass, I. I., "Some aspects of shock-wave research (Dryden lecture)," AIAA J. 25 (1987), pp. 214-229.
3. Glaz, H. M., Colella, P., Glass, I. I., and Deschambault, R. L., "A detailed numerical, graphical and experimental study of oblique shock wave reflections," Lawrence Berkeley Laboratory Report LBL-20033, 1985.
4. Colella, P. and Glaz, H. M., "Efficient solution algorithms for the Riemann problem for real gases," J. Comp. Phys. 59 (1985), pp. 264-289.
5. Colella, P. and Glaz, H. M., "Numerical computation of complex shock reflections in gases," Proc. 9th Intl. Conf. on Numerical Methods in Fluid Dynamics, ed. Soubbaramayer and J. P. Boujot, 1985, Springer-Verlag Lecture Notes in Physics, Vol. 218.
6. Glaz, H. M., Glass, I. I., Hu, T. C. J., and Walter, P., "Oblique shock wave reflections in SF<sub>6</sub>: a comparison of calculation and experiment," AIAA J. Prog. Aero. Astr. 106, Dynamics of Explosions, ed. J. R. Bowen, J.-C. Leyer, and R. I. Soloukhin, 1986, pp. 359-387.
7. Deschambault, R. L., "Nonstationary oblique shocks wave reflections in air," University of Toronto, UTIAS Report No. 270, 1984.
8. Deschambault, R. L. and Glass, I. I., "An update on nonstationary oblique shock wave reflections: actual isopycnics and numerical experiments," J. Fluid Mech. 131 (1983), pp. 27-57.
9. Ben-Dor, G. and Glass, I. I., "Domains and boundaries of non-stationary oblique shock wave reflections. 1. Diatomic Gas," J. Fluid Mech. 92 (1979), pp. 459-496. Also, "2. Monatomic Gas," J. Fluid Mech. 96 (1980), pp. 735-756.

10. Anderson, J., Modern Compressible Flow with Historical Perspective, McGraw-Hill, New York, 1982.
11. Vincenti, W. G. and Kruger, C. H., Introduction to Physical Gas Dynamics, R. E. Krieger Publ. Co., Huntington, NY, 1975.
12. Park, C., "Problems of rate chemistry in the flight regimes of aeroassisted orbital transfer vehicles," AIAA J. Prog. Aero. Astr. 96, Thermal Design of Aeroassisted Orbital Transfer Vehicles, ed. H. F. Nelson, 1985, pp. 511-537.
13. Park, C., "On Convergence of computational chemically reacting flow," AIAA Technical Report 85-0247, 1985.
14. Chern, I. -L. and Colella, P., "Conservative front tracking method for hyperbolic conservation laws," preprint.
15. Colella, P., Ferguson, R. E., Glaz, H. M., and Kuhl, A. L., "Mach reflection from HE-driven blastwave," AIAA J. Prog. Aero. Astr. 106, Dynamics of Explosions, ed. J. R. Bowen, J. -C. Leyer, and R. I. Soloukhin, 1986, pp. 388-421.
16. Hansen, C. F., "Approximations for the thermodynamic and transport properties of high-temperature air," NASA TR R-50, 1959.

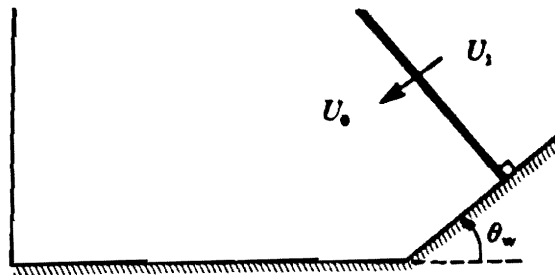


Figure 1. Schematic diagram for flowfield initialization.

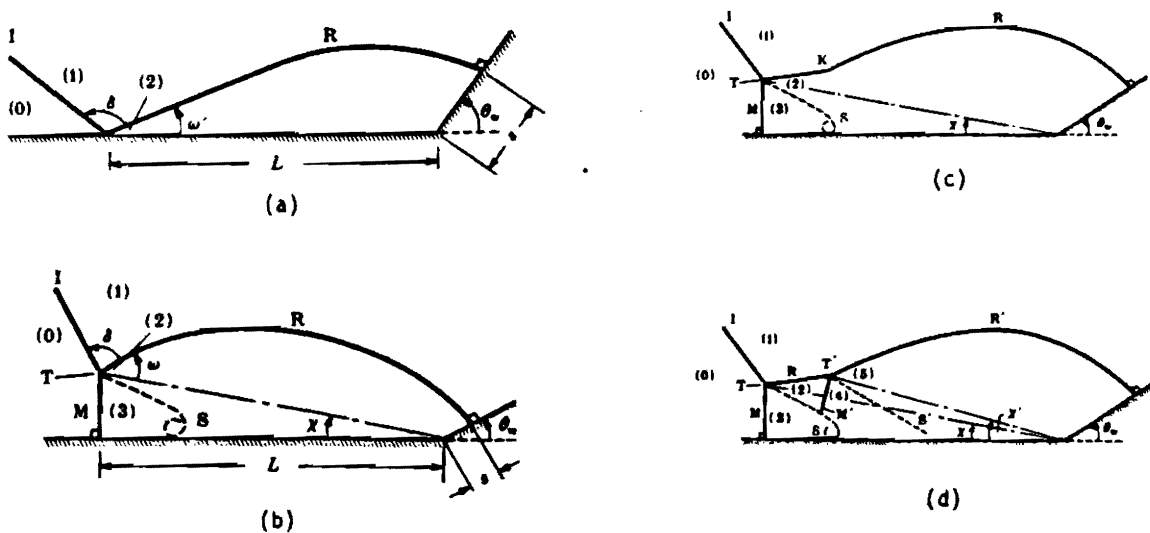


Figure 2. Schematic diagrams of oblique shock-wave reflection types: (a) regular reflection (RR); (b) single Mach reflection (SMR); complex Mach reflection (CMR); double Mach reflection (DMR). States (0), (1), (2), and (3) satisfy the reflection or triple point jump conditions. Other standard terminology used in the text is  $\chi$  = triple point angle, T = triple point, R = reflected shock, I = incident shock, M = Mach stem, T' = second trip point,  $\chi'$  = second triple point angle, M' = second Mach stem, and K = kink.

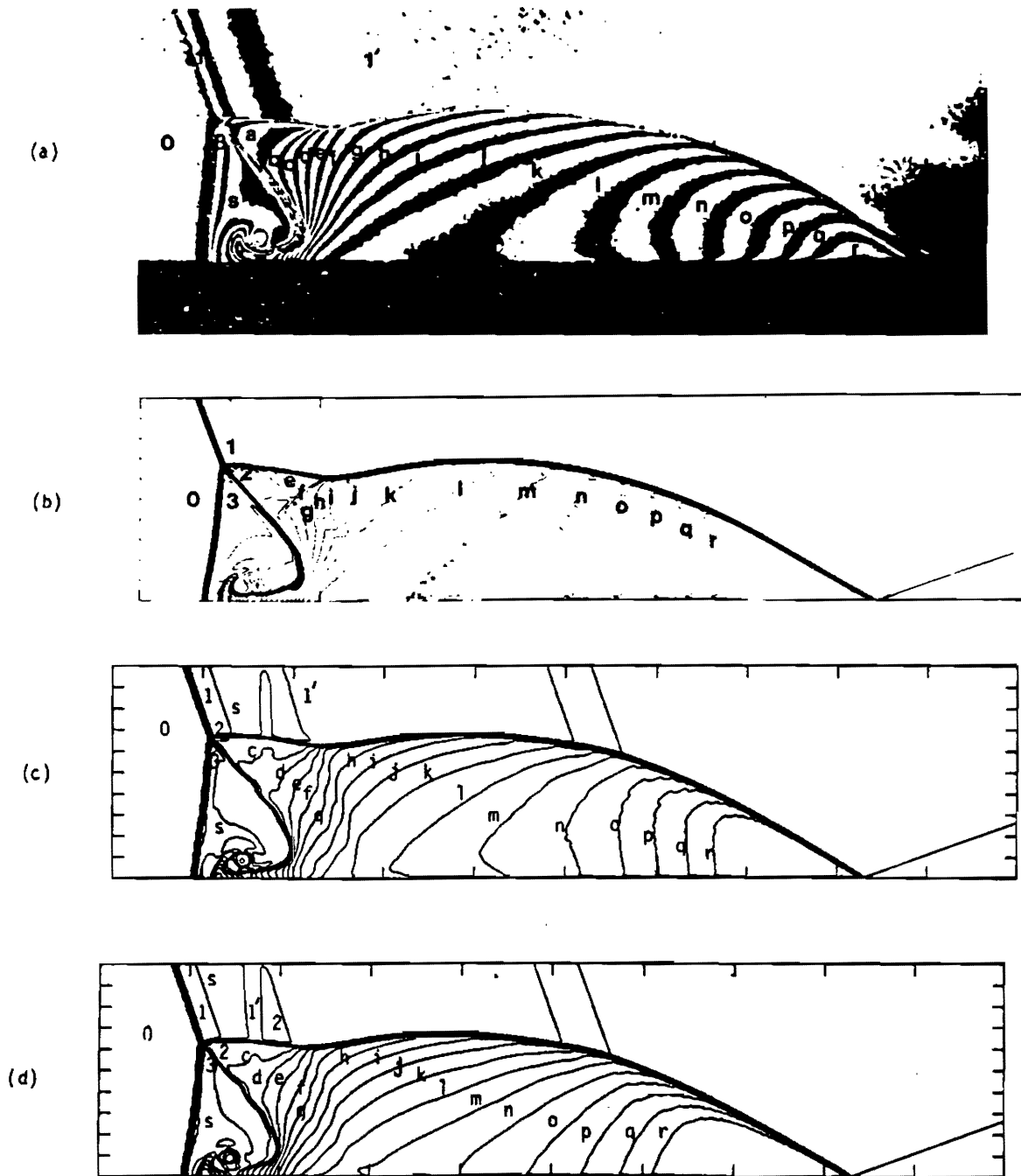


Figure 3.  $M_5 = 7.19$ ,  $\theta = 20^\circ$ . (a) interferogram from experiment; density ( $\rho/\rho_0$ ) contour levels for, (b) gas dynamic calculation using equilibrium EOS, (c) nonequilibrium calculation without reaction, and (d) nonequilibrium, reactive flow calculation. (a), (b) reproduced from Ref. 3, p.196. The values of  $\rho/\rho_0$  are

0	1.00	3	5.59	d	7.94	h	9.24	l	10.53	p	11.82
1	5.47	a	6.97	e	8.27	i	9.56	m	10.85	q	12.15
1'	6.13	b	7.30	f	8.59	j	9.88	n	11.18	r	12.47
2	6.65	c	7.62	g	8.91	k	10.21	o	11.50	s	5.91

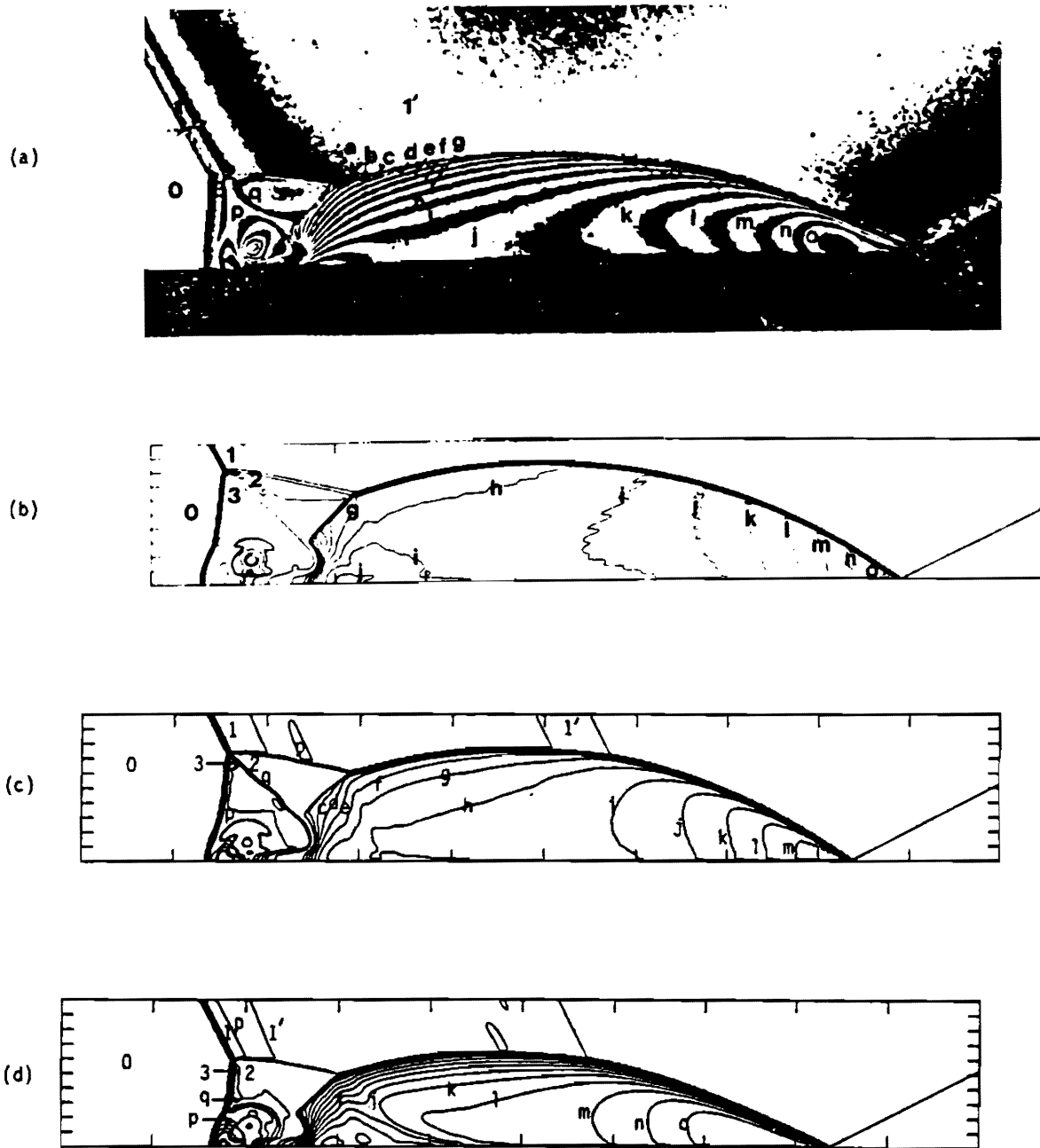


Figure 4.  $M_\infty = 8.70$ ,  $\theta_w = 27^\circ$ . (a) interferogram from experiment; density ( $\rho/\rho_0$ ) contour levels for (b) gas dynamic calculation using equilibrium EOS, (c) nonequilibrium calculation without reaction, and (d) nonequilibrium, reactive flow calculation. (a), (b) are reproduced from Ref. 3, p. 190. The values of  $\rho/\rho_0$  are

0	1.00	3	5.74	d	11.42	h	13.95	l	16.47	o	18.36
1	5.63	a	9.53	e	12.05	i	14.58	m	17.10	p	6.37
1'	6.89	b	10.16	f	12.68	j	15.21	n	17.73	q	8.07
2	7.44	c	10.79	g	13.32	k	15.84				

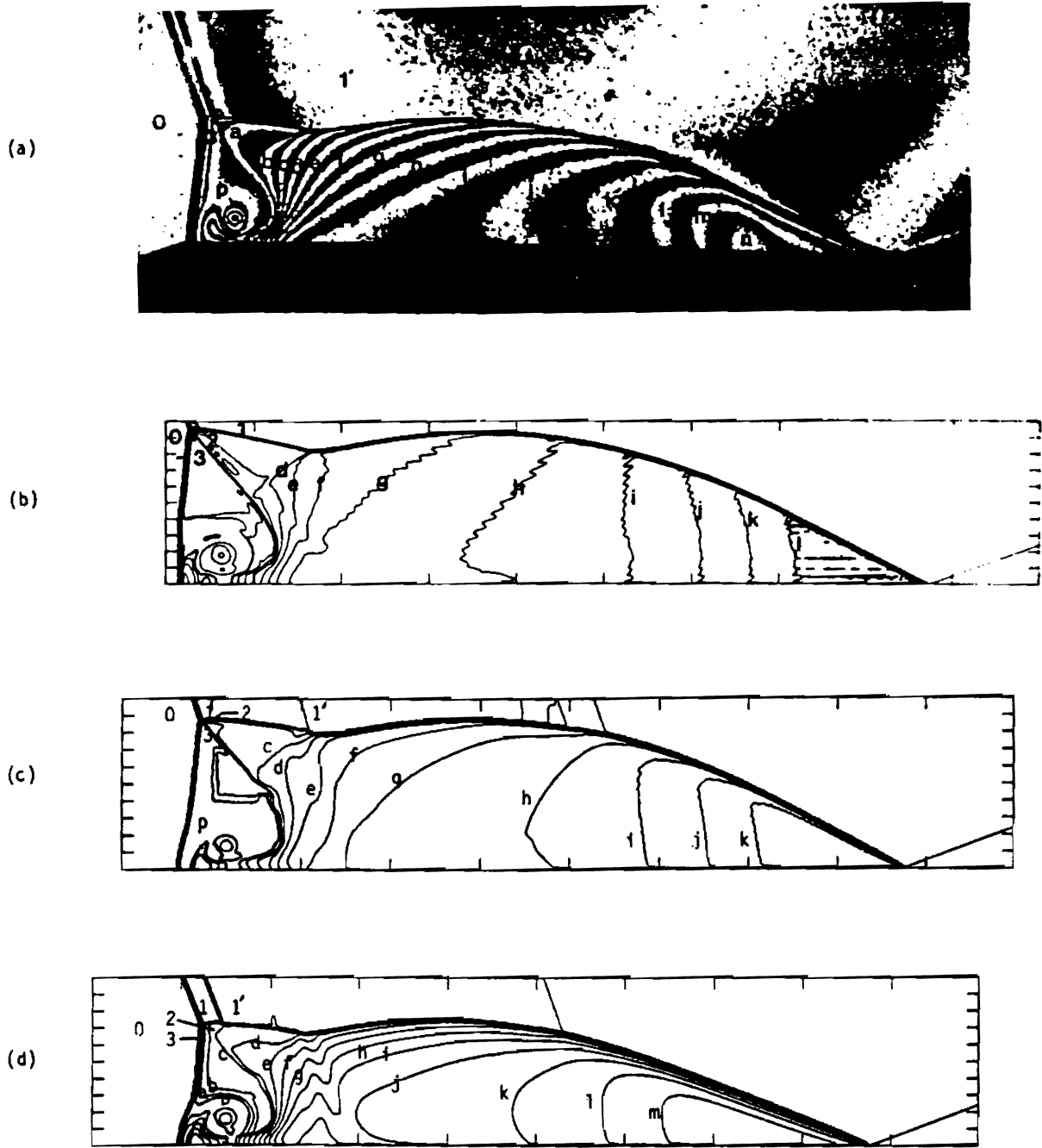
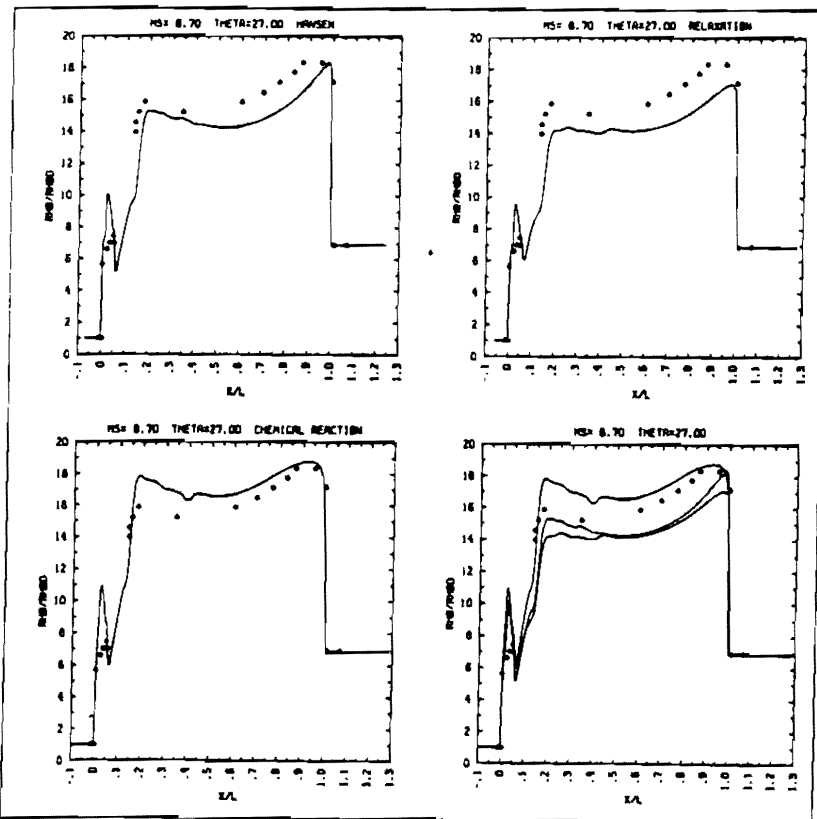
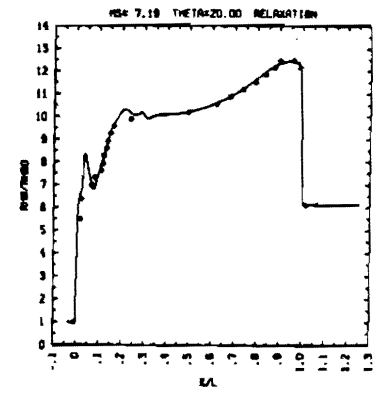
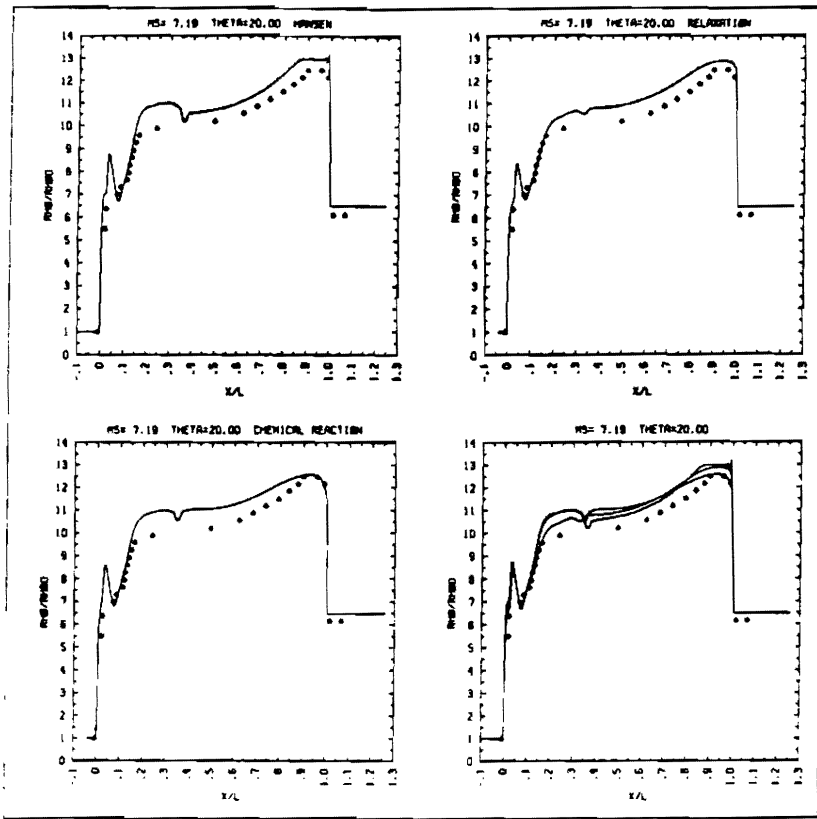


Figure 5.  $M_\infty = 8.86$ ,  $\theta = 20^\circ$ . (a) interferogram from experiment; density ( $\rho/\rho_0$ ) contour levels for (b) gas dynamic calculation using equilibrium EOS, (c) nonequilibrium calculation without reaction, and (d) nonequilibrium, reactive flow calculation. (a), (b) are reproduced from Ref. 3, p. 203. The values of  $\rho/\rho_0$  are

0	1.00	3	5.72	d	9.43	g	11.37	j	13.31	m	15.25
1	5.64	a	7.50	e	10.08	h	12.02	k	13.95	n	15.89
1'	6.93	b	8.14	f	10.73	i	12.66	l	14.60	p	6.85
2	6.85	c	8.79								



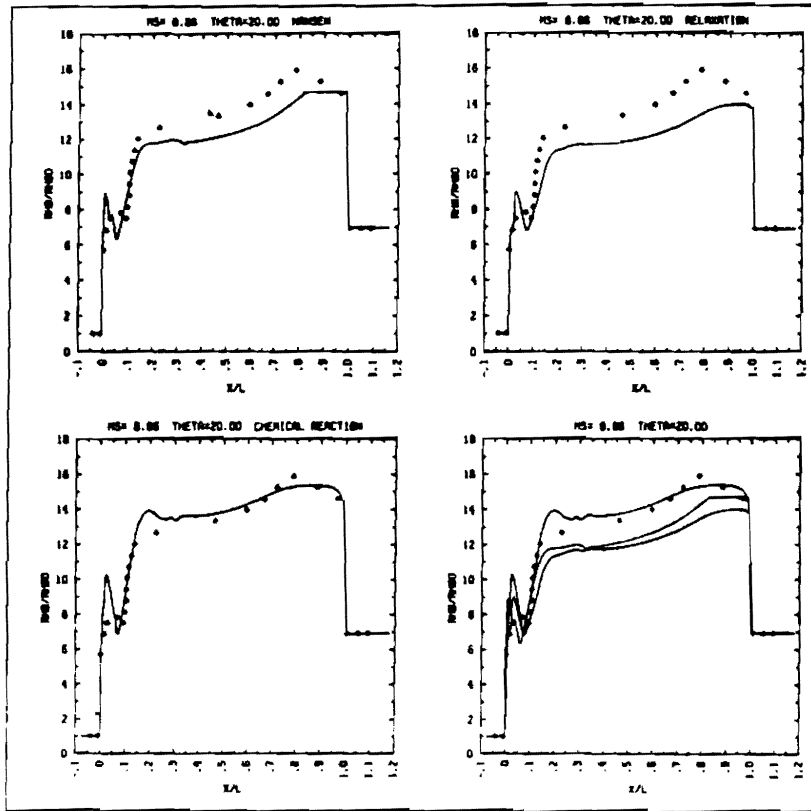


Figure 6. Plots of density vs. distance along the wedge surface for the three cases. See Figures 1, 2 for definition of  $\rho_0$ ,  $L$ . The extra plot for Case I corresponds to the calculation with a forced match in state 1'. Diamonds represent experimental data.



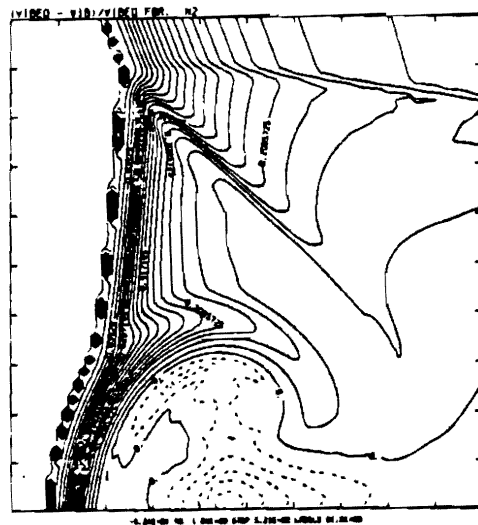
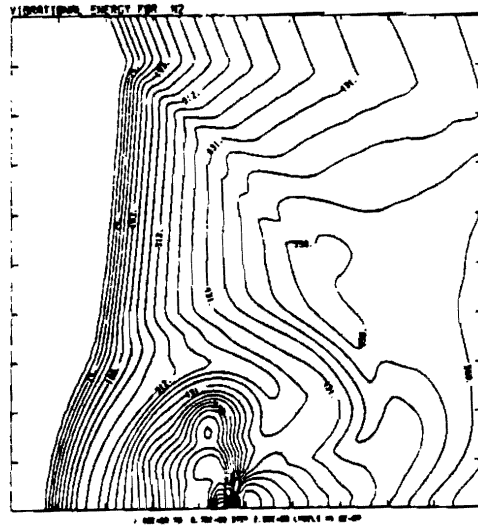
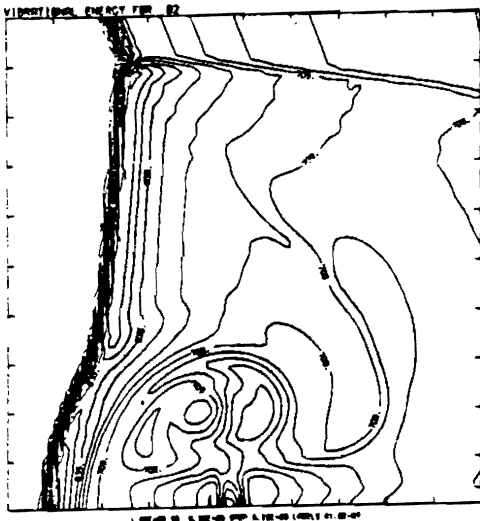
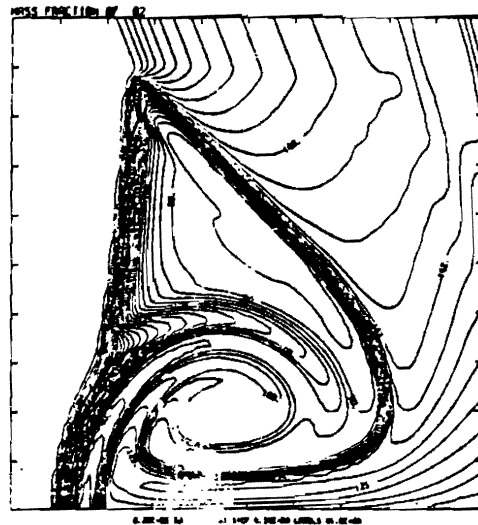


Figure 7. Blowup plots of the Mach stem region for Case III. These plots all use thirty equally spaced contours.